# A parameter study of strato-rotational low-frequency modulations: impacts on momentum transfer and energy distribution

Gabriel Meletti, Stéphane Abide, S Viazzo, U Harlander

## To cite this version:

Gabriel Meletti, Stéphane Abide, S Viazzo, U Harlander. A parameter study of strato-rotational low-frequency modulations: impacts on momentum transfer and energy distribution. Philosophical Transactions of the Royal Society A: Mathematical, Physical and Engineering Sciences, 2023, 10.1098/rsta.2022.0297 . hal-03946442

**HAL Id: hal-03946442**
**https://hal.science/hal-03946442v1**

Submitted on 19 Jan 2023

PHILOSOPHICAL
TRANSACTIONS A

royalsocietypublishing.org/journal/rsta

Research

Article submitted to journal

**Subject Areas:**
fluid mechanics

**Keywords:**
Taylor–Couette flow, Stratified flow, High Performance Computing, Direct Numerical Simulations

**Author for correspondence:**
Gabriel Meletti
e-mail: gabriel.meletti@univ-lyon1.fr

THE ROYAL SOCIETY
PUBLISHING

# A parameter study of strato-rotational low-frequency modulations: impacts on momentum transfer and energy distribution

G. Meletti[1], S. Abide[2], S. Viazzo[3], and U. Harlander[4]

[1]Lyon Institute of Origins LabEx LIO, Université Claude Bernard Lyon 1, Villeurbanne, France
[2]Laboratoire de Mathématiques et Physique, University of Perpignan Via Domitia, Perpignan, France
[3]Laboratoire de Mécanique, Modélisation et Procédés Propre, Aix-Marseille University, CNRS, Centrale Marseille, France
[4]Department of Aerodynamics and Fluid Mechanics, Brandenburg University of Technology (BTU) Cottbus-Senftenberg, Cottbus, Germany.

Previous comparisons of experimental data with non-linear numerical simulations of density stratified Taylor-Couette flows revealed non-linear interactions of strato-rotational instability (SRI) modes that lead to periodic changes in the SRI spirals and their axial propagation. These pattern changes are associated to low-frequency velocity modulations that are related to the dynamics of two competing spiral wave modes propagating in opposite directions. In the present paper, a parameter study of the strato-rotational instability (SRI) is performed using Direct Numerical Simulations to evaluate the influence of the Reynolds numbers, the stratification, and of the container geometry on these SRI low-frequency modulations and spiral pattern changes. The results of this parameter study show that the modulations can be considered as a secondary instability that are not observed for all SRI unstable regimes. The findings are of interest when the Taylor-Couette model is related to star formation processes in accretion disks.

## 1. Introduction

In geophysical and astrophysical flows, stratified vortices that are relevant in the transport of heat and momentum from small to large scales can be observed in stably stratified systems, such as the atmosphere or oceans. In the astrophysical context, accretion disks (from which solar systems are formed) can be seen as stratified vortices. Accretion disks are astrophysical disk-like objects composed of gas and dust that rotate around a central object, like a star. In such systems, understanding the mechanisms that can result in an outward transport of angular momentum is a central problem [19]. For a planet or star to be formed in a disk, angular momentum has to be carried away from its center to allow matter aggregation by gravity; otherwise, the disk's rotation speed would be far too large, avoiding this matter aggregation (and the consequent star formation) to happen. In these gas systems, turbulence is the most likely mechanism to achieve such a large angular momentum transport. However, it was shown that the flow profiles of accretion disks are stable with respect to purely shear instabilities, which arises the question of how turbulence can be generated. Among other candidates, the strato-rotational instability (SRI) has attracted attention in recent years as a possible mechanism to generate turbulence in accretion disks [13, 32]. The SRI is a purely hydrodynamic instability that manifests itself as non-axisymmetric spirals and can be modeled by a classical Taylor-Couette system with stable density stratification [6, 25, 53].

The gas-dust region of accretion disks can be approximated as a simple differentially rotating shear flow – a Taylor-Couette (TC) flow – with near-Keplerian velocity profiles [13]. A classic TC system consists of two concentric cylinders rotating with angular velocities $\Omega_{in}$ and $\Omega_{out}$, and has a mean azimuthal velocity profile $\overline{u_\phi}$ given by

$$\overline{u_\phi(r)} = \Omega_{in} r(\mu - \eta^2) + \frac{r_{in}^2 \Omega_{in}(1-\mu)}{r(1-\eta^2)}, \tag{1.1}$$

where $\mu = \Omega_{out}/\Omega_{in}$ is the rotation ratio between inner and outer cylinders, and $\eta = r_{in}/r_{out}$ is the ratio between inner and outer cylinder radius ($r$). Equation (1.1) is the analytical solution of the hydrodynamic equations in cylindrical coordinates ($\phi$, $r$, $z$) for incompressible Newtonian fluids in infinite long cylinders. When the first term of the right-hand side of (1.1) is zero, the velocity is a potential field, therefore curl-free. This defines the Rayleigh limit, $\mu = \eta^2$, which separates stable from unstable flows in non-stratified TC flows. When $\mu < \eta^2$, the flow is unstable, and Taylor vortices can be observed. If $\mu > \eta^2$, velocity profiles remain stable. In accretion disks, the Keplerian azimuthal angular velocity profile $\Omega(r) \propto r^{-3/2}$ [13] leads to $\mu = \eta^{3/2}$, and hence to a stable flow with respect to the classical TC instability. However, a density stratification could cause a change in the marginal instability transition when compared to classical non-stratified TC systems, making the flow unstable in regions where – without stratification – it would be stable [48]. This characteristic makes the SRI a relevant phenomenon in planetary and astrophysical applications since, as concluded by Dubrulle et al. [13], in astrophysical disks axial stratification due to temperature differences is the rule rather than the exception.

In nature and in laboratory experiments, density stratification can exist due to salinity [6, 25, 40, 53], or to a temperature gradient [48, 49]. Experiments performed by Withjack and Chen [53] found that, unlike the axisymmetric rolls in classic TC flows, the SRI presents non-axisymmetric spirals, confirmed by later experiments performed e.g. by Boubnov et al. [6]. The fact that the SRI manifests itself as non-axissymetric spirals is also relevant for its application to accretion disks theory, given that recent astronomical observations captured spirals in the center of accretion disks at an early stage of a star formation [37], making the study of the SRI spiral signatures and dynamics a relevant topic in this context.

Caton et al. [7] showed by linear stability analysis and experimental observations that the first SRI transition happens via a supercritical Hopf bifurcation that destabilizes purely azimuthal flows. Rüdiger et al. [48] obtained marginal stability curves using linear stability analysis for

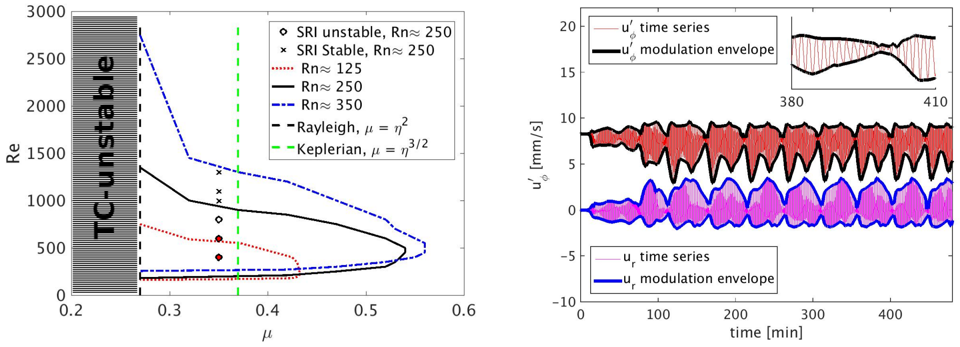

(a) (b)

**Figure 1.** (a) SRI marginal linear stability curves redrawn from Rüdiger et al. [48] for 3 different values of $Rn$. Bigger values of $Rn$ (and $N$) lead to larger instability regions. The black dashed vertical line in the left represents the Rayleigh limit $\mu = \eta^2$, which separates stable and unstable non-stratified TC cases (any to the left of this line in the diagram would be TC unstable, as indicated in the image). The green dashed vertical line in the right represents the Keplerian line $\mu = \eta^{3/2}$. SRI unstable (circles) and stable (crosses) cases for $\eta = 0.517$, $Rn \approx 250$, $\mu = 0.35$ with different Reynolds numbers were investigated numerically and experimentally in Meletti et al. [34]. The circles filled with red color refer to cases for which strong low-frequency amplitude modulations were observed. (b) $u_\phi$ and $u_r$ SRI time series of a numerical simulation presented in Meletti et al. [34], and their respective amplitude envelopes highlighting low frequency amplitude variations within the time interval $0 < t < 8$hours. The results are for $Re = 400$, $\mu = 0.35$ and $\partial T \partial z \approx 5.71\,\mathrm{K/m}$ at mid-gap position ($r \approx r_{in} + d/2$) and mid height position ($z \approx H/2$). The smaller figure inserted on the top-right corner shows a 30 minutes zoomed time-window of $u_\phi$, highlighting how the envelope amplitude variations change much slower than the SRI mode $m = 1$ oscillations.

different values of $Rn$, the Reynolds number based on the buoyancy frequency

$$Rn = N r_{in}(r_{out} - r_{in})/\nu. \tag{1.2}$$

where $\nu$ is the kinematic viscosity of the fluid, and $N$ is the buoyancy frequency, also known as Brunt-Väisälä frequency

$$N = \sqrt{\alpha g \frac{\partial T}{\partial z}}. \tag{1.3}$$

Here, $\alpha$ is the coefficient of thermal expansion, g is the gravity constant, and $\partial T/\partial z$ is the environmental axial temperature gradient. Note that, higher temperature gradients lead to higher values of $N$, and consequently, of $Rn$. Figure 1.(a) reproduces the marginal stability curves redrawn from Rüdiger et al. [48] for different $Rn$ values. Flows inside (outside) these curves are predicted to be SRI unstable (stable). Note that the SRI unstable regions increase with $Rn$. It becomes clear in the diagram that stratified flows with $\mu > \eta^2$ can be unstable (to the right of the Rayleigh limit, shown by the black vertical dashed line). Most important, the Keplerian profile, relevant for accretion disks, can be unstable for all chosen $Rn$ values.

The Reynolds number of the stratified Taylor-Couette flows, presented in the vertical axis of figure 1.(a), is based on the inner cylinder rotation ($\Omega_{in}$), and it is defined as

$$Re = \Omega_{in} r_{in}(r_{out} - r_{in})/\nu. \tag{1.4}$$

The Froude number measures the relative importance of rotation and stratification, being defined as

$$Fr = \frac{Re}{Rn} = \frac{\Omega_{in}}{N}. \tag{1.5}$$

The unstable regions in figure 1.(a) were confirmed by experiments [48, 49], while the upper transition back to stable regimes was captured numerically and experimentally by Meletti et al. [34]. Edlund and Ji [15, 16],

In Meletti et al. [34], experimental and numerical studies at moderate Reynolds numbers revealed low-frequency amplitude modulations resulting from the interaction between SRI spirals travelling in opposite axial directions. These modulations were observed both numerically and experimentally for all velocity components ($u_\phi$, $u_r$, and $u_z$), and in the temperature field $T$. This implies that also the Brunt-Väisälä frequency shows slow variations in time.

The frequency of the modulations, shown in figure 1.(b) and reproduced from Meletti et al. [34], is classified as low-frequency because it is more than 30 times smaller than the SRI frequency (see small image inserted top-right corner of figure 1.(b)). Lopez and Marques [29] also observed numerically that these very low-frequency modulations set in at higher Re, although the main features of the SRI flow remain those of rotating waves. It is also possible to see in figure 1.(b) that the amplitude variations need approximately 100 minutes to achieve a permanent regime. During the transient regime ($t \lesssim 100$ minutes), amplitude variations also exist, but they are not regular in time. It is important to highlight that this mentioned transient regime is related to the amplitude modulations, and not to the SRI oscillations. The SRI oscillations show the mode $m = 1$ peak in the Fourier space [34], and they are already prominent approximately 10 minutes after starting the rotation for all SRI unstable $Re$ values investigated in Meletti et al. [34]. Furthermore, under the assumption of weak Doppler shift, the SRI frequencies assume values between the buoyancy frequency ($N$) and the inertial frequency ($f = 2\Omega_{in}$), while the amplitude modulations have frequencies much below these values, and outside the interval $N - f$. This means that the amplitude modulations cannot be interpreted as low-frequency gravity wave modes.

The analysis of the SRI flow during the amplitude modulations in Meletti et al. [34] also reveals three particular flow patterns that are correlated with the modulations. The patterns represent different SRI spiral inclination and propagation in the axial direction, named downward inclination and upward inclination. During the transition from the upward (downward) to the downward (upward) pattern, both spirals are activated and superposed, leading to a chessboard-type pattern. This transition region is characterized by small SRI amplitudes.

The SRI spirals observed have some similarities with those found in experiments performed by Flór et al. [18] and in numerical simulations performed by Lopez and Marques [28], where two spirals are moving upward and downward resulting in a standing pattern with low-frequency modulations that come from differences in the axial drift speed of the two waves. It should be noted that Flór et al. [18] and Lopez and Marques [28] use a short annulus with a very wide gap for which top and bottom boundary effects and centrifugal buoyancy effects are important. Moreover, in contrast to the investigations presented in Meletti et al. [34] and in the present paper, Lopez and Marques [28] use a smaller Froude number $Fr < 1$ and a larger Reynolds number $Re > 6000$. For longer cavities radiative instability as discussed by Riedinger et al. [45] is relevant as well, as experimental observation of the spiral pattern changes in the axial-radial plane were also revealed.

In view of the variety of experimental and numerical setups, it is important to study the influence of parameter variations on the SRI oscillations and in particular on the occurrence of low-frequency amplitude modulations. Therefore we will use a high performance parallel numerical code to investigate how different parameters can change the behaviour of these experimentally and numerically observed amplitude modulations and pattern changes in the axially travelling spirals. All the cases here explored are for $\mu > \eta^2$, so that the regime is centrifugally stable, but it is unstable with respect to the SRI.

The paper is organized as follows. In section 2, we will investigate how the Reynolds number, geometrical parameters of the cavity (such as its height or gap size), and stronger or weaker stratification in the axial direction can influence the SRI spiral behavior, its mean velocity profiles, and lead to amplitude modulations or suppress it. The evaluation of axially periodic results, with a complete elimination of Ekman effects, is also explored. Section 3 explores how the energy spectra for different SRI regimes can be affected by the presence of the amplitude modulations and how the spectra will change under varying parameters, while section 4 brings an evaluation of its influence on the the SRI turbulent momentum transport in space and time. We will also briefly discuss how this could influence the aggregation of matter by gravity in the center of the disks leading to proto-planetary star formation. Finally, in section 5, conclusions are presented.

## 2. Parameter study

In Meletti et al. [34], SRI amplitude modulations associated with spiral pattern changes were observed numerically and experimentally for a Taylor-Couette system heated from the top, and cooled from the bottom leading to a stable density stratification in the axial ($z$) direction. The observations regarded experiments with Reynolds numbers $Re = 400$ and $Re = 600$, with $\mu = 0.35$ and $\Delta T/\Delta z = 5.71\,\mathrm{K\,m^{-1}}$, but several factors can change the behavior of the axial traveling spirals that lead to the modulations, such as the Reynolds number, the aspect ratio of the cavity, and the strength of the axial stratification. In this section, we will use numerical simulations to investigate how the changes in these parameters can influence the SRI spiral dynamics, i.e. forcing or suppressing amplitude modulations, considering regimes that are centrifugally stable, but unstable with respect to the SRI. The evaluation of axially periodic results, with no influence of Ekman effects, is also explored. Since these SRI phenomena develop at different time scales, it needs to comprehend fine meshes to solve all the scales involved in the problem. Long time integration is also required to investigate long time occurring low-frequency phenomena.

To overcome these difficulties, a direct numerical simulation (DNS) solver combining fourth-order accuracy space discretization and high-performance computing (HPC) has been developed by Abide et al. [2] to investigate the SRI dynamics. The code solves the Navier-stokes equations using the Boussinesq approximation to account for the buoyancy forces. The physical model solved by the code consists on a Taylor-Couette flow configuration filled with an incompressible fluid endowed with a vertical temperature gradient, that leads to a stable density stratification in the axial ($z$) direction. This configuration is the same used by Meletti et al. [34], Seelig et al. [49] to study the SRI experimentally.

Using the Boussinesq approximation to account for the buoyancy forces, the governing equations solved by the code read:

$$\left\{\begin{array}{ll} \nabla \cdot \mathbf{u} = 0 & \text{in } D, \\ \partial_t \mathbf{u} + (\,\mathbf{u} \cdot \nabla)\ \mathbf{u} = -\nabla p + \nu \Delta\ \mathbf{u} + \mathbf{F} & \text{in } D, \\ \partial_t T + (\mathbf{u} \cdot \nabla) T = \kappa \nabla^2 T & \text{in } D, \end{array}\right. \tag{2.1}$$

where $D$ is the computational domain, $\kappa$ the fluid thermal conductivity, $p$ is the pressure, $T$ is the temperature field, and $\mathbf{u} = (u_r, u_\phi, u_z)$ is the velocity vector field in radial, azimuthal and axial directions, respectively. The body force $\mathbf{F}$ is the buoyancy force driven by density variation:

$$\mathbf{F} = \alpha\, \mathbf{g} \frac{\partial T}{\partial z} \Delta z. \tag{2.2}$$

In the simulations presented here, the velocity is prescribed at the cylinders' walls. The upper and bottom boundaries rotate with the same angular velocity of the outer wall. The vertical temperature gradient results from the temperature difference $\Delta T$ imposed between the top and bottom lids. Considering that there is no relevant heat losses through the lateral walls compared to the thermal forcing at the top and bottom lids, we impose adiabatic boundary conditions at the lateral walls. The simulations are initiated using randomly distributed small amplitude white noise perturbations, to drive the development of the instabilities. Also, centrifugal buoyancy [28, 29] was assumed to not play a significant role in the experiments, and it is not included in the numerical model. The smallest space resolution considered in the simulations was of $32 \times 64 \times 200$ grid points, respectively in the $\phi \times r \times z$ directions.

The time discretization is made using the methods proposed by Hugues and Randriamampianina [23]. Higher-accuracy space discretization is presently achieved through the spectral Fourier

| Case | $Re$ | $\mu$ | $H$ [mm] | $r_{in}$ [mm] | $r_{out}$ [mm] | Rn | Fr | $\Delta T$ [K] | $\frac{\Delta T}{\Delta z}$ [$\mathrm{K\,m^{-1}}$] |
|---|---|---|---|---|---|---|---|---|---|
| 01) | 400 | 0.35 | 700 | 75 | 145 | 182.7 | 2.2 | 2 | 2.85 |
| 02) | | | | | | 258.4 | 1.5 | 4 | 5.71 |
| 03) | | | | | | 365.4 | 1.1 | 8 | 11.43 |

**Table 1.** Parameters of simulations changing stratification

discretization in the azimuthal direction, and a fourth-order compact finite difference scheme in the two other directions, as presented in Abide and Viazzo [3]. To benefit from the modern High Performance Computing framework, the parallel strategies described in [1] have been implemented, allowing a significant reduction of the total simulation times.

## (a) The role of stratification

To investigate how the stratification can influence the SRI flow, different simulations were compared changing the temperature differences between the top and bottom lids of the TC system keeping $Re = 400$, and the geometrical parameters ($H = 700mm$, $r_{in} = 75mm$, and $r_{out} = 145mm$) fixed. The different parameters investigated are presented in table 1.

The geometrical parameters of reference are chosen to be the same as those of the experimental setup investigated in Meletti et al. [34], where the gap between inner and outer cylinders is filled with a Newtonian M5 silicon oil. The physical properties of the M5 oil at 25 °C, which were also considered in the simulations here presented, are shown in table 2.

**Table 2.** M5 silicone oil properties at $25^oC$

| | | |
|---|---|---|
| kinematic viscosity | $\nu$ | $5 \times 10^{-6}\,\mathrm{m^2\,s^{-1}}$ |
| density | $\rho$ | $923\,\mathrm{kg\,m^{-3}}$ |
| coefficient of thermal expansion | $\alpha$ | $1.04 \times 10^{-3}\,\mathrm{K^{-1}}$ |
| thermal conductivity | $k$ | $0.133\,\mathrm{W\,K^{-1}\,m^{-1}}$ |
| specific heat | $c_p$ | $1630\,\mathrm{J\,kg^{-1}\,K^{-1}}$ |
| Prandtl number | $Pr$ | $\approx 57$ |

In figure 2, we can observe that variations in the axial temperature stratification lead to changes in the axial wavenumber $k$. The wavenumbers were obtained considering non-dimensional wave number at snapshots in the r-z plane, such as those presented in figure 2. Hence $k = 2\pi/\lambda$, where $\lambda = 2\pi\lambda^*/H$ is the non-dimensional wavelength, $H$ is the height of the cavity, and $\lambda^*$ is the dimensional wave length. In figure 2(b), for example, we see that $\lambda^* = H/4$, which implies $k = 4$. For the cases 01, 02, and 03 in table 1 we find axial wavenumbers of $k = 3, 4$ and $k = 7$, showing that changes in the stratification leads to relevant changes in the spirals axial structure.

Figure 3.(a) shows how the azimuthal mean flow changes with stratification. We also see different deviations from the non-stratified TC profile (black dashed line) for higher temperature differences (smaller $Fr$). Note that the deviations form the TC profile are similar for $\Delta T/\Delta z = 5.71\,\mathrm{K\,m^{-1}}$ and $\Delta T/\Delta z = 11.43\,\mathrm{K\,m^{-1}}$ (respectively cases 02 and 03 in table 1), but slightly higher for $\Delta T/\Delta z = 5.71\,\mathrm{K\,m^{-1}}$ (case 02). The deviations from the base flow drop to approximately half its values when the stratification drops to $\Delta T/\Delta z = 2.86\,\mathrm{K\,m^{-1}}$ (cases 01 in table 1). The higher deviations of the base flow when the stratification becomes stronger (smaller $Fr$, and larger $Rn$) can be associated with larger momentum transfers from the inner to the outer region of the gap. A further investigation of the momentum flux will be explored later in section 4, showing that we have a larger momentum transfer driven by the instability when the modulations establish. In figure 3.(b), we see how increasing stratification values has similar impacts in the $\beta$-viscosity, i.e.,

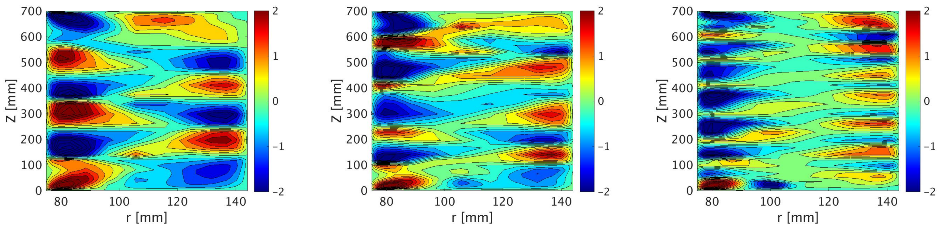

(a) $u_r(\Delta T/\Delta z = 2.86\,\mathrm{K\,m^{-1}})$ (b) $u_r(\Delta T/\Delta z = 5.71\,\mathrm{K\,m^{-1}})$ (c) $u_r(\Delta T/\Delta z = 11.43\,\mathrm{K\,m^{-1}})$

**Figure 2.** Snapshots of $u_r$ in the radial-axial cross section, showing changes in the axial wavenumbers with the temperature gradients. (a) $\Delta T/\Delta z = 2.85\,\mathrm{K\,m^{-1}}$, leading to Froude number $Fr \approx 2.2$; (b) $\Delta T/\Delta z = 5.71\,\mathrm{K\,m^{-1}}$, with $Fr \approx 1.5$; and (c) $\Delta T/\Delta z = 11.43\,\mathrm{K\,m^{-1}}$, with $Fr \approx 1.0$. The Reynolds number of the simulations are $Re = 400$ and rotation the ratios are $\mu = 0.35$.

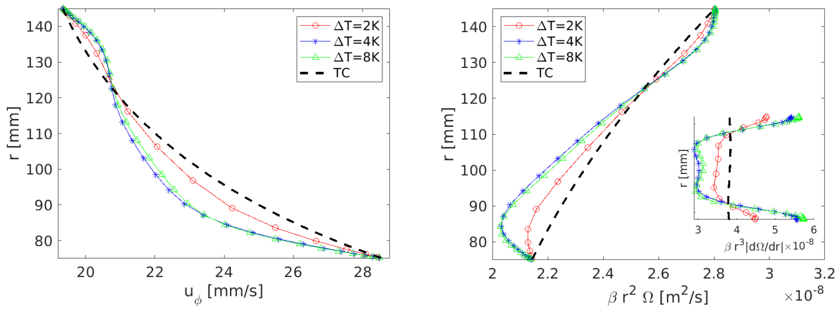

(a) (b)

**Figure 3.** Changes when different temperature gradients in the axial direction are imposed. (a) Mean azimuthal velocity profiles ($\overline{u_\phi}$); (b) Changes in the beta viscosity $\nu_\beta = \beta r^2 \Omega$. The figure inserted on the bottom right corner shows the $\beta$-viscosity defined as $\nu_\beta = \beta r^3 |d\Omega/dr|$ .

we observe larger deviations in the $\beta$-viscosity when the modulations establish. The influence of the stratification in the $\beta$-viscosity is here presented due to its interest in the momentum transfer on Stratorotational instability in Taylor-Couette systems, as well as in accretion disks applications [47]. Note that different definitions of the beta viscosity can be considered. In several publications [24, 31, 43, 44], the beta viscosity is first introduced as $\nu_\beta = \beta r^2 |d\Omega/dr|$, and then the form $\nu = \beta r^2 \Omega$ is presented considering applications to accretion disks and to flows with Keplerian velocity profiles based on laboratory fluid experiment data, where $\beta = 10^{-5}$, $\Omega = u_\phi/r$, and $r$ is the radial position. In figure 3.(b), the $\beta$-viscosity is presented considering these two definitions. In both cases, we observe higher deviations with respect to the stable TC profile when the amplitude modulations establish (higher temperature gradients).

Evaluating the impact of the stratification with respect to the SRI time series (figure 4), we observe that the higher energy transferred from the base flow to the instability is related to the activation of amplitude modulations. By reducing the stratification to half its value keeping all the other parameters constant, the modulation vanish, although the primary SRI instability still exists (see the SRI oscillations in the bottom right figure inside 4(a)). This shows that the SRI can occur without the low frequency amplitude modulations. For the stronger temperature difference $\Delta T = 8\,\mathrm{K}$ (case 03), the modulations are again observed (figure 4(b)). Note that stronger amplitude

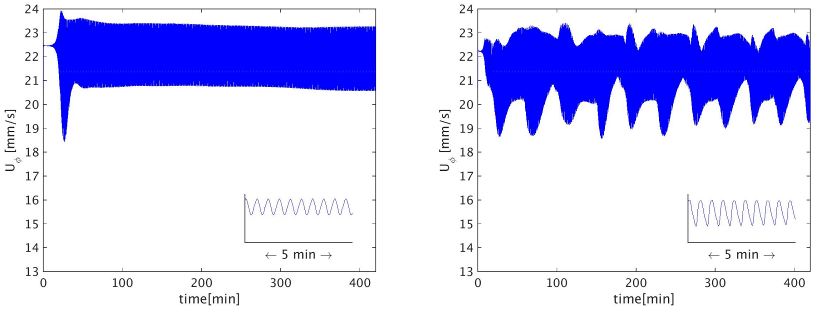

(a) (b)

**Figure 4.** Changes on $u_\phi$ low frequency temporal behaviour when different temperature gradients in the axial direction are imposed, where (a) $u_\phi(\Delta T/\Delta z = 2.85\,\mathrm{K\,m^{-1}})$; (b) $u_\phi(\Delta T/\Delta z = 11.43\,\mathrm{K\,m^{-1}})$. The time series are obtained near the mid-gap and mid-height position ($r \approx r_{in} + d/2$ and $z \approx H/2$), highlighting changes in the low-frequency modulations with the temperature gradient. The smaller images inserted show smaller time intervals of each respective time series (intervals where chosen arbitrarily, in regions where amplitudes do not vary much), highlighting the SRI oscillations. The velocities are presented in the laboratory frame of reference.

modulations are achieved for an imposed temperature difference of $\Delta T = 4\,\mathrm{K}$ and not for $\Delta T = 8\,\mathrm{K}$, added to the fact that $\overline{u_\phi}$ deviations from the TC profile are slightly larger for $\Delta T = 4\,\mathrm{K}$ than for $\Delta T = 8\,\mathrm{K}$ when $\overline{u_\phi} - u_{TC} < 0$ (in the region between $85\,\mathrm{mm} \lesssim r \lesssim 125\,\mathrm{mm}$ on figure 3).

The influence of the stratification in the SRI axial structure moving towards smaller axial wavenumbers $k$ when the Froude number increases can be explained by the work of Rüdiger et al. [48]. They found that the SRI axial length scale ($\lambda_z$), normalized by the gap size $d$, follows the relation

$$\frac{\lambda_z}{d} \simeq \frac{\pi}{4} Fr. \tag{2.3}$$

Larger $Fr$ are obtained when we reduce the stratification (and the values of $N$ become smaller), therefore, will make $\lambda_z$ increase proportionally, corresponding to a dislocation towards smaller axial wavenumbers, until no pattern changes occur, because $\lambda_z$ reaches the same order of $H$. Note that we are not considering Froude numbers that suppress the SRI first instability.

In Meletti et al. [34], we observed that the SRI manifests itself by oscillations associated to a peak in the power spectrum with an azimuthal wavenumber $m = 1$, and weak harmonic interactions occurring between SRI modes. The SRI mode is also observed for the cases here investigated. With values of $\lambda_z \sim \mathcal{O}(H)$, only a suppression of the amplitude modulations are observed, which are near the onset of the instability. Note that we do not observe modulations in regimes that are stable with respect to he SRI, only the opposite, i.e., modulations can establish (or be suppressed) on unstable SRI flows, since the modulations are associated to the SRI spiral axial displacement. Therefore, when no SRI spirals are present in the flow, amplitude modulations do not exist.

## (b) Influence of the Reynolds numbers in the amplitude modulations

On the amplitude, when the Reynolds number is increased from $Re = 400$ to $Re = 800$ (case 06 to case 08 in table 3), keeping $\Delta T/\Delta z$ and $\mu$ unaltered, the modulations disappear, even if the (higher frequency) SRI oscillations are still present. The SRI time series of these simulations, presented in figure 5(a), look similar to other non-modulating cases, such as the case with $Re = 400$ and weaker stratification value of $\Delta T/\Delta z = 2.86\,\mathrm{K\,m^{-1}}$ (case 01 in table 1, figure 2(b)). A chessboard structure establishes in the flows with no modulation and do not change its behavior in time, as highlighted in the space-time diagrams presented in figures 5(b),(c), due to the activation of both positive and

| Case | $Re$ | $\mu$ | $H$ [mm] | $r_{in}$ [mm] | $r_{out}$ [mm] | Rn | Fr | $\Delta T$ [K] | $\frac{\Delta T}{\Delta z}$ [K m$^{-1}$] |
|---|---|---|---|---|---|---|---|---|---|
| 05) | 300 | 0.35 | 700 | 75 | 145 | 258.4 | 1.2 | 4 | 5.71 |
| 06) | 400 | | | | | | 1.5 | | |
| 07) | 600 | | | | | | 2.3 | | |
| 08) | 800 | | | | | | 3.1 | | |
| 09) | 900 | | | | | | 3.5 | | |

**Table 3.** Parameters of simulations changing $Re$

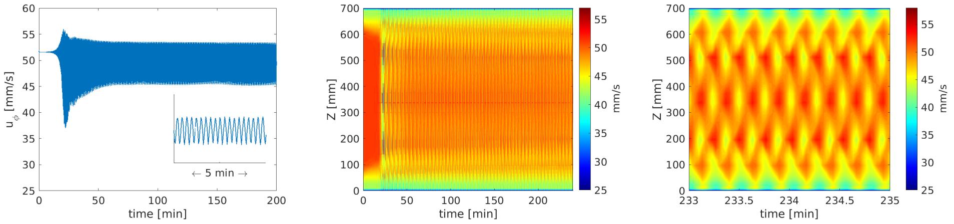

(a) Time-series (b) Full space-time diagram (c) Zoomed space-time diagram

**Figure 5.** $u_\phi$ flow pattern in simulations with Reynolds numbers $Re = 800$ (case 08 in table 3) showing that no amplitude modulations observed. (a) Time-series at a mid-gap and mid-height position. (b) Space-time diagram in the radial-axial cross section during 4 hours of simulations (in physical time). (c) 2 minutes zoomed region highlighting the chessboard patter that establishes and does not change during the full simulation.

negative wavenumbers at the same time, and not a oscillation between the positive and negative modes as we see when we have the modulations (see Meletti et al. [34]). Note that, for $Re = 1000$, the flow becomes stable with respect to the SRI [34]. In both stable cases mentioned (higher Re or smaller $N$), we are near the transition between stable and unstable SRI regimes presented in figure 1.(a). This suggests that the unstable modes related to the secondary instabilities can be activated when we are more inside the instability diagram, far from the transition to stable flow regimes. In other words, too high or too low $Fr$ suppress the modulations. At intermediate $Fr$, the amplitude modulations are activated.

It is relevant to mention that we observed differences with respect to simulations performed by Lopez and Marques [29] for varying Re. These authors observed low frequency modulations at higher Re, while we observe them for smaller Re cases. The modulations disappear when Reynolds numbers are too close to the upper limits of the marginal instability curves presented in figure 1.(a). Note that the previous investigations presented in figure 1.(a) showed how increasing the Reynolds numbers leads to a stable regime with respect to the SRI. We here can highlight that what we observe is the amplitude modulation disappearance, even for unstable SRI regimes.

The comparison with the work of Lopez and Marques [29] comes from the fact that they also observed the transition to the modulated regime in SRI unstable regimes, but coming from lower to higher Reynolds numbers, and not for increasing Re as we observed, indicating that near both the upper or lower boundaries of the marginal instability curves, we have a regime where the SRI instability is activated, but the modulated regime is suppressed. However, in contrast to us Lopez and Marques [29] consider a stationary outer cylinder, with stationary top and bottom walls (only inner cylinder rotation), and we investigate a flow with a Keplerian velocity profile, where the outer cylinder also rotates. The top and bottom cavity lids in our simulations also rotate, with the same angular velocity as the outer cylinder wall, which could have introduced different Ekman effects. Furthermore, Lopez and Marques [29] also take into account centrifugal buoyancy effects

| Case | $Re$ | $\mu$ | $H$ [mm] | $r_{in}$ [mm] | $r_{out}$ [mm] | Rn | Fr | $\frac{\Delta T}{\Delta z}$ [$\mathrm{K\,m^{-1}}$] |
|---|---|---|---|---|---|---|---|---|
| 10) | 400 | 0.35 | 350 | 75 | 145 | 258.4 | 1.5 | 5.71 |
| 11) | | | 700 | | | | | 5.71 |
| 12) | | | 1400 | | | | | 5.71 |
| 13) | | | 2800 | | | | | 5.71 |
| 14) | | | periodic | | | | | 5.71 |
| 15) | | | periodic | | | 365.4 | 1.0 | 11.43 |

**Table 4.** Parameters of simulations changing the cylinder height

that were not considered here because its values become too small in our configuration. Finally, their aspect ratio was small (of $H/d = 3$) in comparison to the $H/d = 10$ values of our simulations. Also important, Lopez and Marques [29] work in smaller Froude number regimes. In view of these differences, a parameter investigation with respect to the geometry and the Ekman effects needs to be addressed next.

## (c) Cavity geometry changes

To understand how the cylinder geometry impacts the SRI and the spiral patterns observed, the cylinder height $H$ is modified from smaller values until an infinitely long cavity (axial periodic boundary condition). We then look at the influence of the cavity gap size $d$ in the SRI development by increasing the distance between the cylinder walls. The parameters of the simulations chosen to investigate the impact of changing the cylinder height are presented in table 4.

### (i) Shorter cavities

Figure 6 shows the result of numerical simulations with $H = 350mm$ (case 10 in table 4), a cavity half as long as the reference height (case 11 in table 4). The reference height is chosen to be of 700 mm, the same as the temperature stratified Taylor-Couette experimental setup presented in Meletti et al. [34]. From the time series related to the chessboard pattern in fig. 6 (full time series not shown) we see that, even if $\Delta T/\Delta z \approx 5.71\,\mathrm{K\,m^{-1}}$ and $Fr \approx 1.5$ in case 10, after a transient phase ($t \gtrsim 100$min), the first SRI instability is established, but the secondary instabilities do not develop. These results are similar to what was observed when the stratification values were reduced to $\Delta T/\Delta z \approx 2.86\,\mathrm{K\,m^{-1}}$ (case 01, in table 1, figure (4(a))). This behavior was also observed when the Reynolds number was increased to $Re = 800$ keeping other parameters constant (case 08 in table 3). In these cases, once the instability was established, the spiral pattern (observed on figure 6) did not change anymore (for the considered simulation time). We think that this suppression of the modulations is related to the fact that larger scales of the flow can not fit in a cavity with length $H = 350mm$ (this will be further described in section 3).

### (ii) Larger cavity heights

Differently from the cavity with reduced length, when the cylinder's height becomes larger than $H_{ref} = 700mm$, the SRI amplitude modulations re-appear. Figure 7(a),(b) show $u_\phi$ time series at $r \approx r_{in} + d/3$ and $z \approx H/2$ respectively to cylinders lengths $2 \times H_{ref}$ ($H = 1400mm$). These pattern changes are associated with (more irregular) amplitude modulations visible in figures 7(c). The amplitude modulations in the time series become less regular as the associated spiral patters also exhibit more complicated behavior than those previously observed for a $H = 700mm$ cavity (reference), with different spiral inclinations existing along the cavities' axial direction. The same conclusion can be obtained for even larger cavities, e.g., for heights four times larger than the reference height ($H = 2800$ mm).

To study the flow in "infinitely long cavities", axially periodic simulations were performed. These are relevant for different reasons, including that many studies investigating the SRI

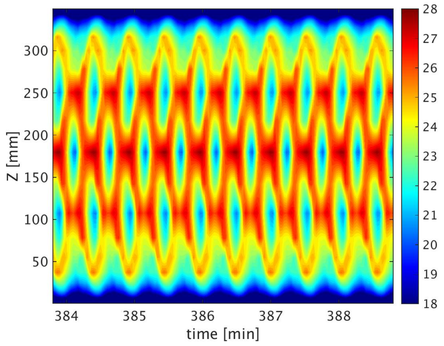

**Figure 6.** $u_\phi$ space-time diagram of a simulation with $Re = 400$, $\mu = 0.35$, $\Delta T/\Delta z \approx 5.71\,\mathrm{K\,m^{-1}}$ and cylinder's height half of the experimental height $H = 0.35m$ (case 10 in table 4) at $r \approx r_{in} + d/3$, showing the standing chessboard pattern achieved when the secondary instability is not reached.

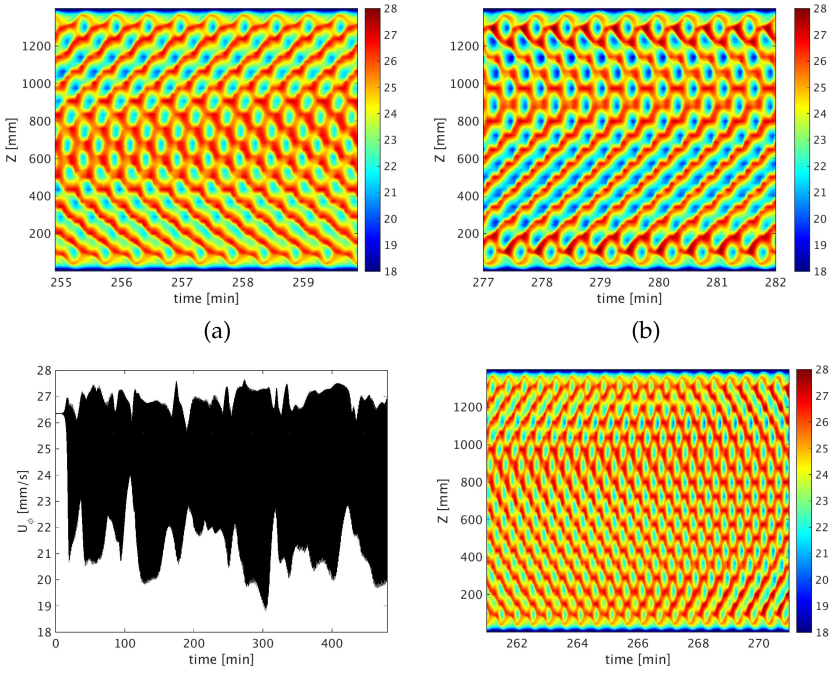

(a) (b)

(c) (d)

**Figure 7.** $u_\phi$ numerical simulations for cavities with twice the height of the experimental setup ($H = 1400\,\mathrm{mm}$) at a fixed radius position $r \approx r_{in} + d/3$, with $\mu = 0.35$ and $\Delta T/\Delta z \approx 5.71\,\mathrm{K\,m^{-1}}$. (a),(b) Space-time diagrams at different time intervals (of 5 minutes) showing the occurrence of different spiral patters in time; (c) $u_\phi$ time series at $z \approx H/2$ of 8 hours interval; (d) Transition from pattern presented in (a) to the pattern in (b).

analytically consider infinitely long cylinders [12, 13, 48]. Note that axially periodic boundary conditions are not necessarily equivalent to infinitely long cavities, but they remove the boundary layer influence on the SRI and the development of amplitude modulations, showing whether Ekman effects could be responsible for the modulations to occur. Furthermore, periodic boundary conditions can also eliminate the possibility of waves and spiral reflections at the top and bottom boundaries leading to the upward and downward traveling spirals.

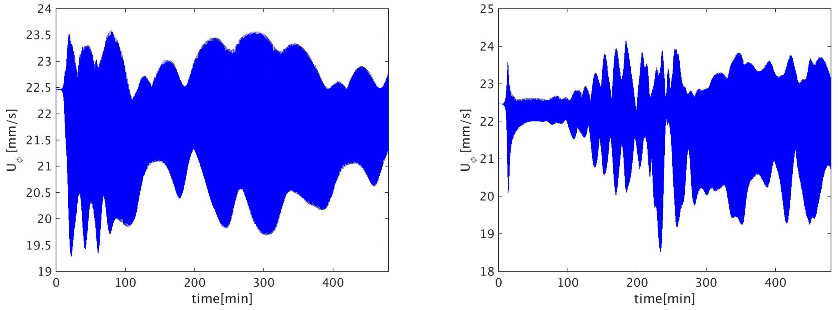

(a) $\Delta T/\Delta z \approx 5.71\,\mathrm{K\,m^{-1}}$ (b) $\Delta T/\Delta z \approx 11.43\,\mathrm{K\,m^{-1}}$

**Figure 8.** $u_\phi$ numerical simulations with $Re = 400$, $\mu = 0.35$ and periodic solutions in the axial direction $z$ ($\Delta z \to \infty$). Time series of 8 hours interval obtained at $r \approx r_{in} + d/2$ and $z \approx H/2$ and (a) temperature gradient $\Delta T/\Delta z \approx 5.71\,\mathrm{K\,m^{-1}}$ (case 14 in table 4); (b) Temperature gradient $\Delta T/\Delta z \approx 11.43\,\mathrm{K\,m^{-1}}$ (case 15 in table 4).

Figure 8 presents $u_\phi$ time series obtained from axially periodic numerical simulations with $Re = 400$, $\mu = 0.35$, and different stratification values. Figure 8(a) with $\Delta T/\Delta z \approx 5.71\,\mathrm{K\,m^{-1}}$ (case 14 in table 4); and 8(b) with $\Delta T/\Delta z \approx 11.43\,\mathrm{K\,m^{-1}}$ (case 15 in table 4). The simulations show that the flow is still unstable when the top and bottom boundaries are removed, and amplitude modulations are still observed in the velocity time series. Pattern changes are once again related to the amplitude modulations. These axially periodic results demonstrate that the secondary instabilities associated with amplitude modulations do not depend on the top and bottom boundaries to exist. They also show that modulations and pattern changes do not result from Ekman pumping effects, since it also occurs without the presence of the lids. Furthermore, the energy transferred from the mean flow to the instability is practically the same for axially bounded or axially periodic periodic simulations (cases 14 and 15 in table 4).

Simulations performed with increasing gap size were also performed, i.e, increasing the distance between inner and outer cylinder radius. Initially, these investigations intended to contribute to the discussion about the importance of a rigid boundary for the SRI to exist, or if critical layers could be activated and generate the instabilities without the need of a rigid outer cylinder wall [12, 26, 39, 52]. The idea to verify if a rigid outer boundary is relevant for the SRI development was simply to increase $d = r_{out} - r_{in}$, and to observe if this would lead to the suppression of the instability.The results, instead, showed only that the changes imposed in $r_{out}$ leads to a delay in the instability development. Therefore, with this simple approach we could not test whether a wider gap will eventually suppress the SRI and SRI modulations or not.

## 3. Energy spectra

In section 2, we observe that larger deviations from the TC profile occur when the secondary instability establishes, compared to cases where only the first instability occurs, showing that more energy is transferred from the base flow. In this section, we will investigate how the kinetic energy spectra are modified for the different regimes observed in section 2.

Three different energy spectra are then considered as function of the wavenumber $K = m, l, k$: one for the azimuthal, another for the radial, and a third one for the axial direction, respectively called $E_\phi$, $E_r$, and $E_z$, keeping fixed the other 2 space coordinates, as detailed in the appendix A. The radial wavenumber is based on the cylinder gap, i.e., in the distance between the inner and outer cylinders. The assumption of 3 different one-dimensional energy spectra is considered as suggested by Billant and Chomaz [5], Lindborg [27].

Figure 9 shows $E_\phi$, $E_r$ and $E_z$ for simulations with $\mu = 0.35$, $\Delta T/\Delta z \approx 5.71\,\mathrm{K\,m^{-1}}$. Figure 9(a) corresponds to $Re = 400$ (case 06 in table 3) and figure 9(b) to $Re = 800$ (case 08 in table 3), with

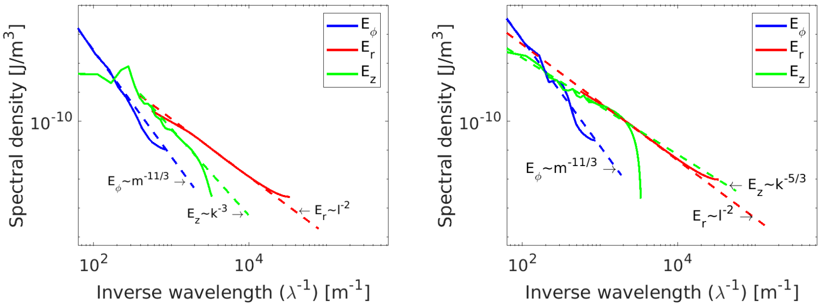

(a) Re=400 (b) Re=800

**Figure 9.** Energy spectra in the azimuthal ($E_\phi$), radial ($E_r$) and axial ($E_z$) directions with different power laws fitting the spectra presented in dashed lines. The spectra were obtained from simulations with $\mu = 0.35$, $\Delta T/\Delta z \approx 5.71\,\mathrm{K\,m^{-1}}$, and bounded cavity height $H = 700mm$. Figure (a) presents a $Re = 400$ simulation where amplitude modulations and pattern changes are observed (case 02 in table 1); (b) shows a simulation with $Re = 800$, where no pattern changes or amplitude modulations occur (case 08 in table 3).

power laws fitting the energy spectra in dashed lines. Note that in the case presented in figure 9(a) the flow develops amplitude modulations, while the case presented in figure 9(b) is simply SRI unstable, but the amplitude modulations do not occur.

In figure 9 we observe different slopes in $E_z$ for cases with and without amplitude modulations. In figure 9(a), with $Re = 400$ and amplitude modulations, $E_z$ has a decay rate proportional to a power law $k^{-3}$. A $k^{-3}$ vertical spectrum ($E_z$) decay can occur on enstrophic cascades [8, 38], which transfers energy from larger to smaller scales in quasi-geostrophic cascade, but may also allow an inverse energy transfer, from smaller to the larger scales. Vertical spectra with $k^{-3}$ decay rate have already been observed on vertical measurements of the atmosphere performed by Cot [9], Dewan and Good [11] and by numerical simulations of strongly stratified fluids by Lindborg [27]. For the case with higher Reynolds number and no amplitude modulation ($Re = 800$) in figure 9(b), a $k^{-5/3}$ power-law fits the $E_z$ decay rate. We find very surprising that a $-5/3$ decay law is observed, since the SRI clearly presents very different features from those of homogeneous isotropic turbulence [14, 41]. This means that its motion excites many wave modes that give rise to a forward energy cascade with a $-5/3$ decay rate, just as in classical Kolmogorov turbulence [10, 46]. It must be highlighted that this $-5/3$ decay does not come from an isotropic turbulent flow regime. According to Lindborg [27], the transition from regimes dominated by strongly stratified environments to regimes dominated by rotation can transform an inverse energy cascade into a purely forward energy cascade. That could explain why, when we increase the Reynolds number (from fig. 10(a) to fig. 10(b)), therefore increasing rotation with respect to stratification, we observe the transition from the $k^{-3}$ decay to a $k^{-5/3}$ cascade behavior.

The power spectra in the radial direction on figure 9 ($E_r$), have slopes with a decay rate proportional to $l^{-2}$. This is the same slope observed by ocean measurements performed by Garrett and Munk [20, 21], related to a random superposition of linear internal waves (i.e., that exist between the inertial frequency $f$ and the buoyancy frequency $N$) known as the Garrett and Munk (GM) model, or related to a weakly nonlinear wave turbulence [4, 30]. Note that, although the GM spectra decay rate of $l^{-2}$ and a $l^{-5/3}$ slope are similar, the $l^{-5/3}$ slope fits very poorly the $E_r$ spectra decay.

A power law $m^{-11/3}$ fits well the slope measured in $E_\phi$ in figures 9(a),(b). This decay has already been associated with different phenomena, such as the influence of potential energy available in turbulent diffusion of quasi-geostrophic cascades [51], or with Kelvin waves propagating along a vortex line [33]. Curiously, in an astrophysics context, $m^{-11/3}$ power law was measured over a broad length-scale domain in energy spectra of diffuse molecular clouds surrounding young stars [17], as well as proposed in a MHD context [35]. These astrophysical observations were performed in the North Celestial Pole loop, which has a cylindrical gap morphology, with a cylindrical radial velocity profile fitting its radial expansion [36]. Here, it is important to be stressed that the mechanisms that lead to the power laws observed still remain to be further explored using theoretical approaches. Only then, any possible relation between them and astrophysical and geophysical measurements could be established.

The power laws that fit the energy decay in $E_\phi$ and $E_r$ do not change when we compare figures 9(a) and (b), i.e., no changes in their decay rates are observed when the amplitude modulations are established or suppressed. No relevant changes in $E_\phi$ and $E_r$ were observed for changes in any of the different parameters investigated, i.e., from numerical simulations with different Reynolds number, with different stratification values (different $\Delta T$ and $Rn$), or for different cavity heights $H$ (bottom images). We observed a small increase in the $E_\phi$ and $E_r$ total energy with the Reynolds number, that dislocate the spectra in the y-axis without changing their shapes, but no other relevant changes in the radial and azimuthal energy spectra were noticed with changes in the stratification, height or $Re$, and the spectra decay rates of $E_\phi$ and $E_r$ remain similar to those observed in figures 9(a),(b).

In the axial energy spectra $E_z$, presented in figures 9(a) and 9(b), besides the changes in decay rates, we can observe the presence of a peak in the spectra with $Re = 400$, that is not observed for simulations with $Re = 800$. In figure 10, we show axial energy spectra $E_z$ changes with stratification, Reynolds numbers, and with the cavity height. We can then evaluate which signatures of the SRI and of the spiral propagation in $z$ (and modulations) can be observed, i.e., to see which modes are activated in $E_z$ when the spiral propagation occurs, and how the different parameters investigated in section 2 can change the energy transfer from the base flow to the unstable modes. In figure 10, the x-axis presents the axial wavenumber $k$. Smaller figures were introduced on the top right corner of each image showing the inverse wavenumber ($\lambda^{-1}$) in the x-axis, and with the spectra arbitrarily dislocated in the y-axis for better visualization of the results. The relation between $\lambda$ and the wave numbers are given by

$$m = \frac{2\pi}{\lambda_\phi}, \; l = \frac{2\pi}{\lambda_r}, \; k = \frac{2\pi}{\lambda_z}. \tag{3.1}$$

On figure 10(a), the changes in $E_z$ with the Reynolds number are evaluated, maintaining the stratification constant ($\partial T/\partial z \approx 5.71\,\mathrm{K\,m^{-1}}$, and $Rn \approx 258.4$). It is possible to observe that, for $Re = 300$, $Re = 400$, and $Re = 600$, where the amplitude modulations and pattern changes are observed, a peak in $E_z$ is also observed. This peak is associated with an injection of energy from the base flow to the instability at a certain wavenumber. As the Froude number increases and rotation becomes stronger compared to the stratification, the peak moves to smaller wavenumbers (and to larger scales), until it disappears for $Re = 800$, where no modulation is observed. Reducing the stratification leads to similar results, i.e., reducing $\Delta T$ and making $Fr$ larger also leads to a dislocation of the peaks in the direction of the larger scales (smaller wavenumbers).

In figure 10(c), we observe $E_z$ changes with the cylinder's height, and peaks in $E_z$ are observed when changes in the spiral patterns occur. For $H = 350mm$, i.e., half of the reference height, where the SRI is observed with no amplitude modulations (see section i), the peak in $E_z$ is not present. Although the wavenumber increases with the cylinder's height, the image on the top right corner of figure 10(c) shows that changing $H$ did not change the wavelength, and also that larger scales are not able to develop in the smaller height cavity (of $H = 350mm$), leading to the suppression of the spiral pattern changes in $z$. When "infinite heights" are simulated, i.e., axial periodic boundary conditions on figure 10(d), weak non-linearities start to appear, with harmonics in the $E_z$ spectra. Note that, although no pattern changes are observed in the periodic simulations with $\Delta T/\Delta z \approx 5.71\,\mathrm{K\,m^{-1}}$ in section (c), relatively strong amplitude modulations were present, and peaks in the $E_z$ spectrum are also observed in this case. Also note that the reference simulation with $Re = 400$, $\mu = 0.35$, $\Delta T = 4K$, and $H = 700mm$, has a peak associated to the wavenumber $k = 4$, as well as the unbounded axially periodic simulations (also with $H = 700mm$).

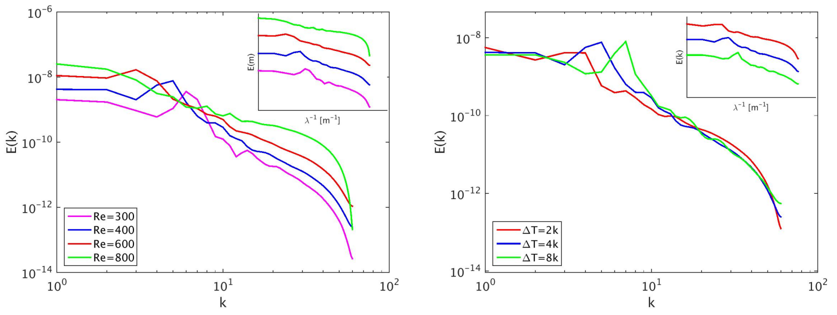

(a) Changing $Re$

(b) Changing $\Delta T$

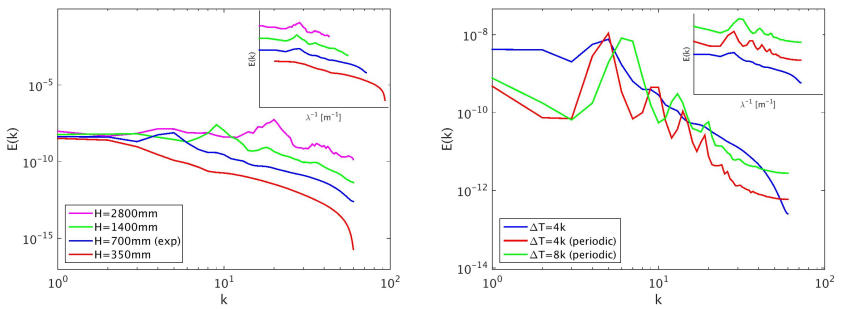

(c) Changing $H$

(d) Changing $\Delta T$ and top/bottom BC

**Figure 10.** Energy spectra in the axial direction ($E_z$). (a) Different $Re$, for fixed $H = 700\,\mathrm{mm}$, $\Delta T = 4\,\mathrm{K}$. (b) Different stratification ($\Delta T$), with fixed $Re = 400$, and $H = 700\,\mathrm{mm}$. (c) Different cylinder's heights, with fixed $Re = 400$ and $\Delta T/\Delta z \approx 5.71\,\mathrm{K\,m^{-1}}$; (d) Comparison of axial periodic and non-periodic top and bottom boundary conditions; The x-axis in all figures present the axial wavenumber $k$. The smaller figures inserted on the top right corner of each image show the spectra arbitrarily dislocated in the y-axis for better visualization of the results, and have the inverse wavelength ($\lambda^{-1}$) in the x-axis, instead of the wavenumber $k$. All simulations were performed with $\mu = 0.35$.

The influence of rotation, stratification, and height in the SRI axial structure, observed as a peak in the energy spectra on figures 10 moving towards smaller axial wavenumbers $k$ when the Froude number increases, can be explained once again by the work of Rüdiger et al. [48]. Equation (2.3) showed that the length-scale of the SRI axial structure grows linearly with the Reynolds number, and is inversely proportional to the buoyancy frequency. As mentioned in section (a), a larger $Fr$ will then make $\lambda_z$ increase, corresponding to a dislocation towards smaller axial wavenumbers, until no pattern changes occur in simulations with $Re = 400$ and half of the reference cavity height ($H = 350mm$), or with $Re = 800$ and the same reference cavity height ($H = 700mm$) because $\lambda_z$ reaches the same order as $H$. Once again, we note here that, differently from what is proposed by Rüdiger et al. [48], a suppression of the SRI first instability was not observed here when $\lambda_z \sim \mathcal{O}(H)$. What we observe is the suppression of the amplitude modulations.

## 4. Impacts of the modulations on the SRI momentum transport

In this section, we will investigate the SRI momentum transport in time. This is an important issue regarding how the SRI could transport momentum outwards from the center of accretion disks, leading to proto-planetary star formation.

The $u'_\phi u'_r$ spatial structure behaviour (not shown), such as increasing axial wavenumbers with the stratification (similar to what was observed for the velocity spiral axial profiles in figure 2),

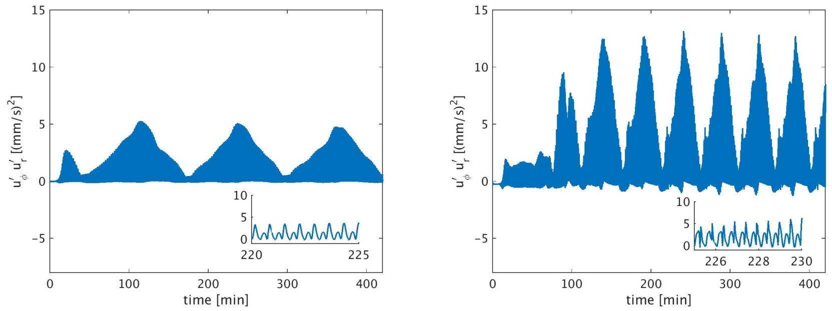

(a) $Re = 300$ (b) $Re = 400$

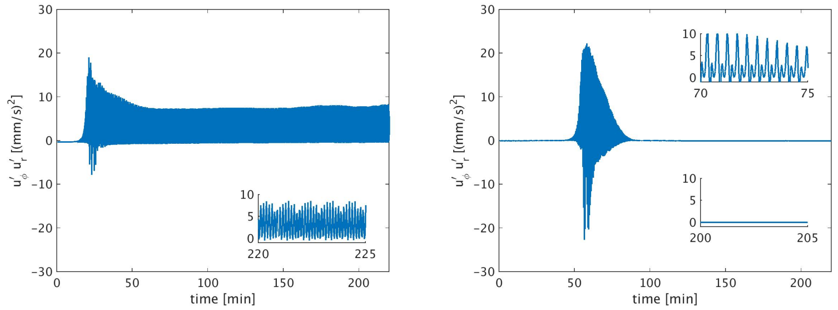

(c) $Re = 800$ (d) $Re = 900$

**Figure 11.** $u'_\phi u'_r$ time series for increasing Reynolds number with a fixed temperature gradient $\Delta T/\Delta z = 5.71\,\mathrm{K\,m^{-1}}$. The velocities are obtained at position $r = 90\,\mathrm{mm}$ (near the inner cylinder) and $z \approx H/2$ (mid-height). Note time of the upper figures (a),(b) is of $0 \leq t \leq 420$ minutes, and of the bottom images (c),(d) are of $0 \leq t \leq 220$ minutes. The small figures inserted show the SRI oscillations in a 5 minutes time window. Figure (d) has two inserted figures, when the SRI occur at the transient phase ($t < 90$ minutes) and another inserted image after the flow becomes stable (for $t > 90$ minutes).

shows that SRI related momentum should be carried by the SRI spirals. Since momentum transfer within the flow is related to the spiral structure, it is relevant to show how the previously observed amplitude modulations, associated with the spiral axial propagation, will affect the $u'_\phi u'_r$ temporal behavior. Figure 11 shows $u'_\phi u'_r$ time series for numerical simulations with constant stratification ($\Delta T/\Delta z = 5.71\,\mathrm{K\,m^{-1}}$) and different Reynolds numbers. The values of $\mu = 0.35$ and $H = 700\,\mathrm{mm}$ are kept constant in all results presented in this section, and the time series are obtained, either on a fixed space position at mid-height cavity ($z = H/2$), or near the inner cylinder, since we are interested in understanding how momentum could be affected close to the center in accretion disks (associated here to the inner cylinder region). Note that the top figures 11(a),(b) present results in the time interval $0 \leq t \leq 400$ minutes, while the time interval on figures 11(c),(d) are smaller, varying from $0 \leq t \leq 220$ min. For Reynolds numbers $Re = 300$, $Re = 400$ (figures 11(a),(b)), and $Re = 600$ (not shown) and fixed $\Delta T/\Delta z = 5.71\,\mathrm{K\,m^{-1}}$ (and for larger $N$ values), low frequency amplitude modulations in $u'_\phi u'_r$ are observed, indicating that, for intermediate values of the Froude number, momentum can indeed be transferred in bursts. The frequency of the amplitude modulations increase with the Froude number, until it reaches a regime where no amplitude modulation occurs, leading to a continuous momentum transfer, as seen in figure 11(d). Zoomed intervals of 5 minutes in $u'_\phi u'_r$ time series are presented inside each image of figure 11, to highlight the presence of the higher frequency SRI oscillations.

The modulations observed in the momentum transport may have an impact on accretion disk theory taking into account that constant or intermittent regimes might lead to different conditions of how matter collapses in the center of the disks. Note that signatures of an intermittent transport

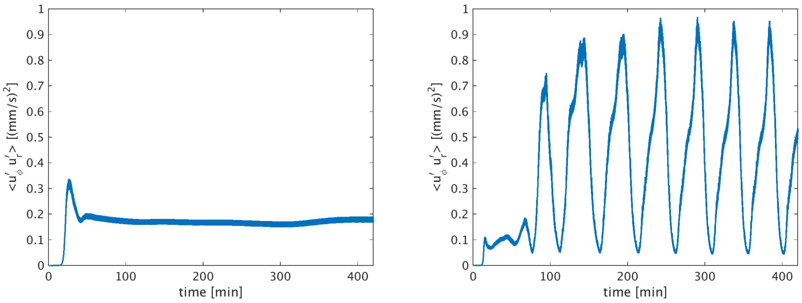

(a) $\Delta T/\Delta z \approx 2.86\,\mathrm{K\,m^{-1}}$ (b) $\Delta T/\Delta z \approx 5.71\,\mathrm{K\,m^{-1}}$

**Figure 12.** Time series of the azimuthal space mean $\left\langle u'_{\phi} u'_{r} \right\rangle$ at a fixed radial position very close to the inner cylinder wall ($r \approx 76.14\,\mathrm{mm}$ while inner cylinder radius is at $r_{in} = 75\,\mathrm{mm}$) and mid-height axial position $z \approx H/2$. The results are from numerical simulation with different stratification values ($\Delta T/\Delta z$) and with the same $Re = 400$, $\mu = 0.35$, $d = 70mm$ and $H = 700mm$ (cases 01 and 02 in table 1).

was already measured in astrophysical contexts, such as in the measurements of molecular clouds in the north Celestial pole loop performed by Falgarone et al. [17], where the turbulent energy dissipation was reported to occur in bursts [36]. These systems guard some similarities with the SRI geometry, such a cylindrical gap morphology, and energy spectra of dust clouds surrounding young stars with decay rates of $k^{-11/3}$ (the same decay rate of $E_{\phi}$ obtained in the numerical simulations presented in section 3). It is important to highlight that the modulations impact how momentum is transfer in time (in a continuous or in a burst regime), but the $\beta$-viscosity [24, 44] presented in figure 13(a) shows that, on average, the SRI momentum transfer growths with the Reynolds numbers, i.e., that, on average, the angular momentum transport for the cases here evaluated depends linearly on the shear [22] .

Other time-dependent momentum transfer regimes are observed in the amplitude modulation transient regions in figures 11, for $t \lesssim 100$ minutes, before a more regular amplitude modulation is established. In figure 11(d), when the Froude number reaches approximately 3.5, the transition region has a relevant impact in the momentum transfer. For time $\gtrsim 90$ minutes, the flow is stable, but in the interval $50 \lesssim t \lesssim 90$ minutes, a burst of momentum transfer occurs. This phenomenon might be important for accretion disks applications, as that could allow a proto-planetary star to form at the early stage of the SRI development, even in cases where the regime achieves stability for $t \to \infty$. According to Shtemler et al. [50], shear flow mechanisms may give rise to transiently growing perturbations in accretion disks, while the work of Rebusco et al. [42] shows that there would be enough time for these small perturbations to grow significantly by a few orders of magnitude and for secondary SRI instabilities to develop (such as the amplitude modulations) before viscous or non-linear effects take over and suppress the instability. Yecko [54] examined viscous three-dimensional linear disturbances associated with Keplerian accretion disk-like flows, and predicted that non-modal disturbances can lead to large transient amplification factors, that can make asymptotically stable flows transiently unstable. In figure 12(a),(b), the temporal behavior of the spatial mean in the azimuthal direction, $\left\langle u'_{\phi} u'_{r} \right\rangle$, is presented. The average is performed at a fixed radial position near the inner cylinder, and at an axial position far from the end-gap boundaries. These results show how the net outward flux of momentum at a given radial position (near the inner cylinder) will be constantly outwards, but also that it will occur in bursts when the amplitude modulations are activated, and continuously when no pattern changes occur. In figure 13, we can see that the net flux of $\left\langle u'_{\phi} u'_{r} \right\rangle$ is positive considering all the cavity height (in the axial direction), and that it increases for cases where the modulations are established. This

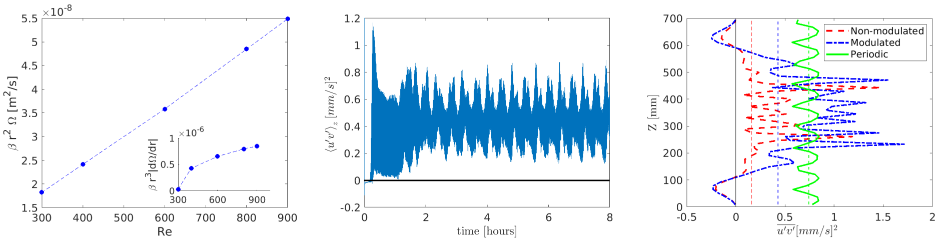

(a) (b) (c)

**Figure 13.** Axial structure (in the $z$ direction) of the momentum transfer at a fixed mid-gap radial position. (a) $\beta$-viscosity growth (with the Reynolds number) averaged in time and along the axial ($z$) direction, considering the definitions $\nu_\beta = \beta r^2 \Omega$ and $\nu_\beta = \beta r^3 |d\Omega/dr|$ (in the image inserted in the bottom right corner); (b) $\left\langle u'_\phi u'_r \right\rangle_z$ time series averaged along the axial ($z$) direction for the case with $Re = 400$, $\mu = 0.35$, $\Delta T/\Delta z \approx 5.71\,\mathrm{K\,m^{-1}}$, and $H = 700mm$ (case 01 in table 1). (c) $\left\langle u'_\phi u'_r \right\rangle_z$ averaged in time comprehending a non-modulated case, one modulated, and one case with axial periodic boundary condition (respectively cases 01, 02 and 14). The dashed vertical lines show the axial space average (along $z$) of the curves presented.

behavior was observed for any different radial position near the inner cylinder, to all simulations evaluated where the SRI was established (with or without the amplitude modulations).

## 5. Conclusions

The main results of the parameter study can be summarized as follows:

(i) The SRI does not necessarily lead to amplitude modulations. Low frequency modulations can be activated at values that are inside the SRI linear stability diagram, and they can be suppressed when we reach regions closer to stable regimes. Analysing the changes in both the Reynolds numbers and the buoyancy frequency, we then conclude that the modulations are established at intermediate Froude numbers, i.e., it is suppressed if $Fr$ becomes either too high or too low.

(ii) The amplitude modulations were shown too disappear when the length of the cavity (cavity height H) was reduced to half of its initial value, and reappeared with more irregular behaviour when the cavity is enlarged with respect to its original reference length.

(iii) Simulations with periodic boundary conditions at the bottom and top lids also led to the development of the secondary instability, showing that the presence of lids is not a necessary condition for the modulations and the pattern transitions to occur.

(iv) With respect to the energy spectra, the power laws that fit the energy decay in $E_\phi$ and $E_r$ do not change with the SRI regime, i.e., no relevant changes in their decay rates are observed with or without the establishment of the amplitude modulations. The power spectra in the radial direction ($E_r$) have a decay rate proportional to $l^{-2}$, that could be related to a random superposition of linear internal waves (the Garrett and Munk (GM) model).

(v) For the axial energy spectra $E_z$, changes in the spectral slope were observed when the secondary instability establishes. When the modulations are present, the decay rate of $E_z$ inertial range is proportional to a power law $k^{-3}$. When only the first SRI instability is achieved and no amplitude modulations occur, a power law with a decay rate $-5/3$ is observed. For $E_z$, besides the changes in their decay rates, the presence of a peak can be observed when the secondary instability occurs. As the Froude number increases and rotation becomes stronger compared to the stratification, the peak dislocates to smaller wavenumbers (larger scales), until it disappears when no modulation is observed. For periodic boundary conditions, weak non-linearities are observed in the kinetic energy spectra, with harmonics in $E_z$.

(vi) The spacial structure of the momentum transport $u'_\phi u'_r$ for different stratification values ($\Delta T$, or $Rn$) shows that the momentum transport in the SRI is carried by the spirals. The amplitude modulations associated with the spiral axial propagation also affects $u'_\phi u'_r$ temporal behavior. Low-frequency amplitude modulations in $u'_\phi u'_r$ were observed showing that, for intermediate Froude numbers, the SRI net momentum transfer can indeed show intermittency and can happen in the form of bursts.

Although only a first step, the parameter study presented is relevant to better classify the occurrence of low-frequency oscillations in a flow with shear, rotation and stratification, i.e. a flow rather typical in the geophysical context. The complex spatio-temporal behavior of stratified Taylor-Couette flow might also help interpret data from astrophysical disks that recently revealed unexpectedly rich dynamical behavior.

## Acknowledgements.

Gabriel Meletti and Uwe Harlander acknowledge the financial support from the DFG core facility center 'Physics of rotating fluids', DFG HA 2932/10-1, and from the Graduate School of BTU Cottbus-Senftenberg and of the Aix Marseille University. Further, the support of a French-German cotutelle program by Aix Marseille University and BTU Cottbus-Senftenberg is gratefully acknowledged. The authors thank also the Deutscher Akademischer Austauschdienst (DAAD), Germany, and Ministère des Affaires Étrngères, France, for the financial support in the frame of the PROCOPE project PHC 46672RE. The authors thank Isabelle Raspo, Anthony Randriamampianina for many helpful discussions and constant support of our work and Torsten Seelig and Andreas Krebs for help with the data analysis.

# References

1 S Abide, M S Binous, and B Zeghmati. An efficient parallel high-order compact scheme for the 3d incompressible navier–stokes equations. *International Journal of Computational Fluid Dynamics*, 31(4-5):214–229, 2017.
2 S Abide, S Viazzo, I Raspo, and A Randriamampianina. Higher-order compact scheme for high-performance computing of stratified rotating flows. *Computers & Fluids*, 174:300–310, 2018.
3 Stéphane Abide and Stéphane Viazzo. A 2d compact fourth-order projection decomposition method. *Journal of Computational Physics*, 206(1):252–276, 2005.
4 KR Allen and RI Joseph. A statistical mechanical explanation of the garrett and munk model of oceanic internal waves. *John Hopkins APL Technical Digest*, 10(4):348–361, 1989.
5 Paul Billant and Jean-Marc Chomaz. Self-similarity of strongly stratified inviscid flows. *Physics of fluids*, 13(6):1645–1651, 2001.
6 BM Boubnov, EB Gledzer, and EJ Hopfinger. Stratified circular couette flow: instability and flow regimes. *Journal of Fluid Mechanics*, 292:333–358, 1995.
7 François Caton, Béatrice Janiaud, and Emil J Hopfinger. Stability and bifurcations in stratified taylor–couette flow. *Journal of Fluid Mechanics*, 419:93–124, 2000.
8 Jule G Charney. Geostrophic turbulence. *Journal of the Atmospheric Sciences*, 28(6):1087–1095, 1971.
9 Charles Cot. Equatorial mesoscale wind and temperature fluctuations in the lower atmosphere. *Journal of Geophysical Research: Atmospheres*, 106(D2):1523–1532, 2001.
10 Edmond M Dewan. Stratospheric wave spectra resembling turbulence. *Science*, 204(4395): 832–835, 1979.
11 EM Dewan and RE Good. Saturation and the "universal" spectrum for vertical profiles of horizontal scalar winds in the atmosphere. *Journal of Geophysical Research: Atmospheres*, 91(D2): 2742–2748, 1986.
12 S LE Dizès and X Riedinger. The strato-rotational instability of Taylor–Couette and Keplerian flows. *J. Fluid Mech*, 660:147–161, 2010.

13 B Dubrulle, L Marié, Ch Normand, D Richard, F Hersant, and J.-P Zahn. An hydrodynamic shear instability in stratified disks. *Astronomy & Astrophysics*, 429:1–13, 2004.

14 Bérengère Dubrulle. Beyond kolmogorov cascades. *Journal of Fluid Mechanics*, 867, 2019.

15 Eric M Edlund and Hantao Ji. Nonlinear stability of laboratory quasi-keplerian flows. *Physical Review E*, 89(2):021004, 2014.

16 Eric M Edlund and Hantao Ji. Reynolds number scaling of the influence of boundary layers on the global behavior of laboratory quasi-keplerian flows. *Physical Review E*, 92(4):043005, 2015.

17 Edith Falgarone, Benjamin Godard, and Pierre Hily-Blant. Turbulence in the diffuse interstellar medium. *Proceedings of the International Astronomical Union*, 7(S280):187–202, 2011.

18 Jan-Bert Flór, Lionel Hirschberg, BH Oostenrijk, and Gert Jan F van Heijst. Onset of centrifugal instability at a rotating cylinder in a stratified fluid. *Physics of Fluids*, 30(8):084103, 2018.

19 Sébastien Fromang and Geoffroy Lesur. Angular momentum transport in accretion disks: a hydrodynamical perspective. *arXiv preprint arXiv:1705.03319*, 2017.

20 Christopher Garrett and Walter Munk. Space-time scales of internal waves. *Geophysical Fluid Dynamics*, 3(3):225–264, 1972.

21 Christopher Garrett and Walter Munk. Space-time scales of internal waves: A progress report. *Journal of Geophysical Research*, 80(3):291–297, 1975.

22 M Gellert and G Rüdiger. Stratorotational instability in Taylor–Couette flow heated from above. *J. Fluid Mech*, 623:375–385, 2009.

23 Sandrine Hugues and Anthony Randriamampianina. An improved projection scheme applied to pseudospectral methods for the incompressible navier–stokes equations. *International Journal for Numerical Methods in Fluids*, 28(3):501–521, 1998.

24 J-M Huré, Denis Richard, and J-P Zahn. Accretion discs models with the $\beta$-viscosity prescription derived from laboratory experiments. *Astronomy & Astrophysics*, 367(3):1087–1094, 2001.

25 M. Le Bars and P. Le Gal. Experimental analysis of the stratorotational instability in a cylindrical couette flow. *Physical Review Letters*, 99(6):064502, 2007. ISSN 00319007.

26 Geoffroy Lesur. *Instabilités et sources locales de turbulence dans les disques d'accrétion*. PhD thesis, Université Joseph-Fourier-Grenoble I, 2007.

27 Erik Lindborg. The energy cascade in a strongly stratified fluid. *Journal of Fluid Mechanics*, 550: 207–242, 2006.

28 Juan M Lopez and Francisco Marques. Impact of centrifugal buoyancy on strato-rotational instability. *J. Fluid Mech*, 890(A9), 2020.

29 Juan M Lopez and Francisco Marques. Stratified taylor–couette flow: nonlinear dynamics. *Journal of Fluid Mechanics*, 930, 2022.

30 Yuri V Lvov, Kurt L Polzin, and Esteban G Tabak. Energy spectra of the ocean's internal wave field: Theory and observations. *Physical review letters*, 92(12):128501, 2004.

31 Donald Lynden-Bell and Jim E Pringle. The evolution of viscous discs and the origin of the nebular variables. *Monthly Notices of the Royal Astronomical Society*, 168(3):603–637, 1974.

32 Wladimir Lyra and Orkan M Umurhan. The initial conditions for planet formation: Turbulence driven by hydrodynamical instabilities in disks around young stars. *Publications of the Astronomical Society of the Pacific*, 131(1001):072001, 2019.

33 Victor S L'vov and Sergey Nazarenko. Spectrum of kelvin-wave turbulence in superfluids. *JETP Letters*, 91(8):428–434, 2010.

34 G. Meletti, S. Abide, S. Viazzo, A. Krebs, and U. Harlander. Experiments and long-term high-performance computations on amplitude modulations of strato-rotational flows. *Geophysical & Astrophysical Fluid Dynamics*, 0(0):1–25, 2020.

35 Philipp Mertsch and Subir Sarkar. Loops and spurs: The angular power spectrum of the galactic synchrotron background. *Journal of Cosmology and Astroparticle Physics*, 2013(06):041, 2013.

36 H Meyerdierks, A Heithausen, and K Reif. The north celestial pole loop. *Astronomy and Astrophysics*, 245:247–256, 1991.

37 Gabriela A Muro-Arena, Christian Ginski, Carsten Dominik, Myriam Benisty, Paola Pinilla, AJ Bohn, T Moldenhauer, Wilhelm Kley, D Harsono, Thomas Henning, et al. Spirals inside the millimeter cavity of transition disk sr 21. *Astronomy & Astrophysics*, 636:L4, 2020.

38 GD Nastrom and K So Gage. A climatology of atmospheric wavenumber spectra of wind and temperature observed by commercial aircraft. *Journal of the atmospheric sciences*, 42(9):950–960,

1985.

39 Junho Park. *Waves and instabilities on vortices in stratified and rotating fluids*. PhD thesis, Ecole Polytechnique X, 2012.

40 Junho Park and Paul Billant. The stably stratified Taylor–Couette flow is always unstable except for solid-body rotation. *Journal of Fluid Mechanics*, 725:262–280, 2013.

41 Stephen B Pope. *Turbulent flows*. Cambridge university press, 2000.

42 Paola Rebusco, Orkan M Umurhan, W Kluźniak, and Oded Regev. Global transient dynamics of three-dimensional hydrodynamical disturbances in a thin viscous accretion disk. *Physics of Fluids*, 21(7):076601, 2009.

43 Denis Richard and Sanford S Davis. A note on transition, turbulent length scales and transport in differentially rotating flows. *Astronomy & Astrophysics*, 416(3):825–827, 2004.

44 Denis Richard and Jean-Paul Zahn. Turbulence in differentially rotating flows what can be learned from the couette-taylor experiment. *Astronomy & Astrophysics*, 1999.

45 X. Riedinger, S. Le Dizés, and P. Meunier. Radiative instability of the flow around a rotating cylinder in a stratified fluid. *Journal of Fluid Mechanics*, 672:130–146, 2011. doi: 10.1017/S0022112010005938.

46 James J Riley and Stephen M DeBruynkops. Dynamics of turbulence strongly influenced by buoyancy. *Physics of Fluids*, 15(7):2047–2059, 2003.

47 G Rüdiger and D A Shalybkov. Stratorotational instability in MHD Taylor-Couette flows. *Astronomy & Astrophysics*, 493:375–383, 2009.

48 G Rüdiger, T Seelig, M Schultz, M Gellert, Chr Egbers, and U Harlander. The stratorotational instability of Taylor-Couette flows of moderate Reynolds numbers. *Geophysical & Astrophysical Fluid Dynamics*, 111(6):429–447, 2017.

49 T Seelig, U Harlander, and M Gellert. Experimental investigation of stratorotational instability using a thermally stratified system: instability, waves and associated momentum flux. *Geophysical & Astrophysical Fluid Dynamics*, 112(4):239–264, 2018.

50 Yu M. Shtemler, M. Mond, G. Rüdiger, O. Regev, and O. M. Umurhan. Non-exponential hydrodynamical growth in density-stratified thin Keplerian discs. *Monthly Notices of the Royal Astronomical Society*, 406(1):517–528, 2010. ISSN 00358711.

51 KS Smith, G Boccaletti, CC Henning, I Marinov, CY Tam, IM Held, and GK Vallis. Turbulent diffusion in the geostrophic inverse cascade. *Journal of Fluid Mechanics*, 469:13, 2002.

52 Chen Wang and Neil J Balmforth. Strato-rotational instability without resonance. *Journal of Fluid Mechanics*, 846:815–833, 2018.

53 EM Withjack and CF Chen. An experimental study of Couette instability of stratified fluids. *Journal of Fluid Mechanics*, 66(4):725—-737, 1974.

54 PA Yecko. Accretion disk instability revisited-transient dynamics of rotating shear flow. *Astronomy & Astrophysics*, 425(2):385–393, 2004.

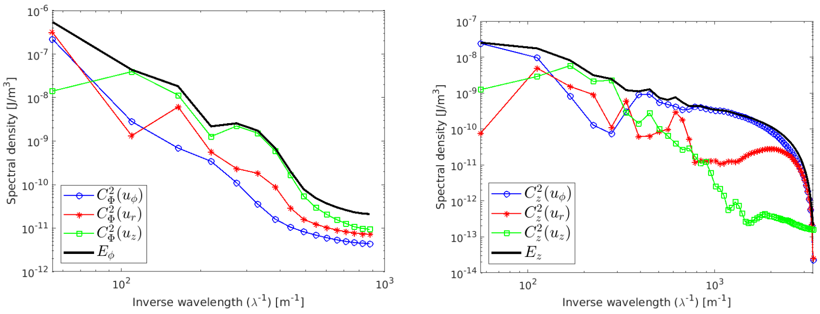

(a) $E_\phi$ (b) $E_z$

**Figure 14.** Space spectra obtained from each velocity component ($C^2_\xi(u_\phi)$, $C^2_\xi(u_r)$, and $C^2_\xi(u_z)$) highlighting each individual contribution to the energy spectrum in (a) azimuth and (b) axial directions. $C^2_\xi$ denotes the multiplication of each $C_\xi$ by its complex conjugate $C^*_\xi$. The full thick black lines correspond to the spectra obtained considering the 3 different velocity components, calculated using A 1. The spectra are obtained from simulations corresponding to case 08 in table 3, with $\mu = 0.35$ and $\Delta T/\Delta z \approx 5.71\,\mathrm{K\,m^{-1}}$, bounded cavity height $H = 700mm$, and $Re = 800$, where no pattern changes or amplitude modulations occur.

# A. Energy spectra computation

The energy spectra are considered for different spatial directions. To obtain each spectrum, the Fourier transform of the velocity components is computed in each space direction (equivalent to the spectra of the velocity fluctuations $u'_\phi$, $u'_r$, and $u'_z$). The assumption of one-dimensional energy spectra is considered as suggested by Billant and Chomaz [5], Lindborg [27]. The energy spectra are then computed as

$$\begin{aligned}
E_\phi &= \frac{1}{2}\rho\left(C_\phi(u_\phi)C^*_\phi(u_\phi) + C_\phi(u_r)C^*_\phi(u_r) + C_\phi(u_z)C^*_\phi(u_z)\right) d\phi d\phi,\\
E_r &= \frac{1}{2}\rho\left(C_r(u_\phi)C^*_r(u_\phi) + C_r(u_r)C^*_r(u_r) + C_r(u_z)C^*_r(u_z)\right) drdr, \qquad \text{(A 1)}\\
E_z &= \frac{1}{2}\rho\left(C_z(u_\phi)C^*_z(u_\phi) + C_z(u_r)C^*_z(u_r) + C_z(u_z)C^*_z(u_z)\right) dzdz,
\end{aligned}$$

where $C_\phi(u_\xi)$, $C_r(u_\xi)$ and $C_z(u_\xi)$ are the fast Fourier transform of $u_\xi = u_\phi$, $u_r$, and $u_z$, with the sub-index indicating respectively the space directions $\xi = \phi$, $r$, and $z$, and $C^*_\xi$ is the complex conjugate. In equation (A 1), $d\phi$, $dr$, and $dz$ are the space resolution of the numerical simulation grid respectively in the azimuth, radial and axial directions. Three different energy spectra are then obtained as function of the wavenumber $K = m, l, k$: one for the azimuthal, another for the radial, and a third one for the axial direction, respectively called $E_\phi$, $E_r$, and $E_z$, keeping fixed the other 2 space coordinates. The contribution of each individual velocity fluctuation to the spectra in the azimuthal ($E_\phi$) and axial ($E_z$) directions are shown in figures 14(a),(b).

The spectra in the azimuth direction ($E_\phi$) were computed at fixed radial and axial position $r \approx r_{in} + d/2$ and $z \approx H/2$. In the radial direction, $E_r$ was computed for fixed $\phi = 0$ and $z \approx H/2$, and in the axial direction, $\phi = 0$ and $r \approx r_{in} + d/2$ are fix. The power density spectra presented in this section are computed for each time step, and then temporally averaged, i.e., the results are the time-mean spectrum of each spectrum obtained. Additionally, the transition period of the amplitude modulation was not taken into account.